Integrated approach to stainless steel 316L parts repair for pitting corrosion using laser metal deposition

Bilel Si Smail, Thomas Cailloux, Yann Quinsat, Wilfried Pacquentin, Srikanth Narasimalu, Hicham Maskrot, Fanny Balbaud-Celerier

Integrated approach to stainless steel 316L parts repair for pitting corrosion using Laser Metal Deposition

Bilel Si Smail[1], Thomas Cailloux[2], Yann Quinsat[1], Wilfried Pacquentin[2], Srikanth Narasimalu[3], Hicham Maskrot[2], Fanny Balbaud-Celerier[4]

[1]*LURPA, ENS Paris-Saclay, Université Paris-Saclay, 91190 Gif-sur-Yvette, France*
[2]*Université Paris-Saclay, CEA, Service d'Etudes Analytiques et de Réactivité des Surfaces (SEARS), 91191, Gif-sur-Yvette, France*
[3]*Energy Research Institute @ NTU, Nanyang Technological University, 50 Nanyang Avenue, Singapore 639798, Singapore*
[4]*Université Paris-Saclay, CEA, Service de la Corrosion et du Comportement des Matériaux dans leurs Environnement (SCCME), 91191, Gif-sur-Yvette, France*

Abstract

With the development of additive manufacturing (AM) and in particular laser metal deposition (LMD), new possibilities for the repair of damaged metal components are developing. In this context, the use of AM offers an efficient way to restore functionality to a defective part, especially for high value parts. In this study, a numerical chain is proposed to automate the repair process of stainless steel naval parts affected by pitting corrosion. An ellipsoidal repair volume is generated at each iteration by intersecting the nominal surface and the ellipsoid surface, which initial dimensions are those of the pitting corrosion defect. This optimization considers dimensional and technical constraints, which results in minimizing the repair volume in order to reduce manufacturing time and costs. Finally, repair tests are performed on ellipsoidal pre-machining, in order to observe the influence of the surface conditions and the pattern deposition on the final quality of the repair (porosity, microstructure and microhardness). The repaired parts highlight a heterogeneous microstructure and microhardness. The surface condition of the pre-machining has no influence on the repair. However, the deposition pattern influences the presence of porosities and the microhardness value in the deposit.

Highlights

- LMD was used to repair ellipsoidal pre-machining with optimized parameters from SS316L powder.
- Numerical optimization minimizes the repair volume to eliminate pit, while respecting dimensional and technical constraints.
- The heterogeneous microstructure of the repair results in heterogeneous mechanical properties
- No influence of the surface condition of the pre-machining on the final quality of the repair

Keywords: Additive manufacturing, laser metal deposition, repair, pitting corrosion, SS316L

1. Introduction

1.1. Context

The service life of mechanical parts depends on various factors. In the context of use in an aggressive environment, corrosion can be a penalizing element [1]. In fact, a localized area with corrosion can lead to the rejection of the part. Corrosion can occur within several forms, depending on the factors surrounding the part or the part itself [2]. The form of corrosion is related to the homogeneity of the environment and/or of the part. Here are some types that corrosion can take: general corrosion, pitting corrosion, intergranular corrosion, and galvanic corrosion [2].

Pitting corrosion is frequent for stainless steels immersed in seawater [3]. This type of localized corrosion can lead to perforation of the part. It occurs when there is a break in the passive film of the part which can be due to an external mechanical action. The exposed part acts as an anode that will transmit electrons to the rest of the material, which functions as a cathode through an electrolytic solution. It also results in a deep degradation of the material, often invisible to the human eye, which can cause severe damage to a functional component.

Brijder *et al.* [4] show that pitting corrosion occurs on all critical parts in air or under

water. Similarly, the state of the art established by Bhandari *et al.* [5] highlights that the pitting phenomenon is usually very localized and deep in stainless steel parts and is difficult to detect.

According to several articles that deal with pitting corrosion in stainless steels (SS), the shape can be considered as a semi-ellipsoid. In fact, The work of Ernst *et al.* [6] to understand the growth of corrosion pits on SS304 reveals the ellipsoidal shape of the pits (Figure 1 (a)). More recently, this shape for corrosion pits has been supported by research on corrosion in the oil and gas industry [7] (Figure 1 (b)). On the other hand, Eguchi, *et al.* [8] propose a semi-ellipsoidal shape to characterize this type of corrosion with parameters a, b and c define the dimensions of the pitting, as can be seen in Figure 1 (c).

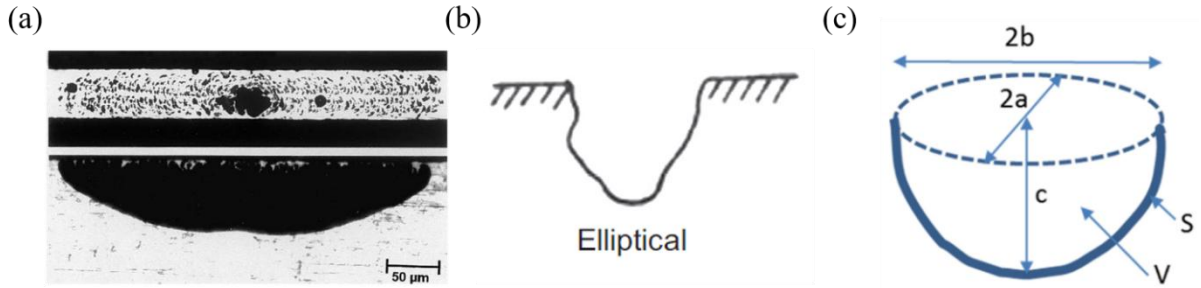

Figure 1. Pitting corrosion shape highlighted by (a) Ernst *et al.* [6], (b) Obeyesekere *et al.* [7], (c) Eguchia *et al.* [8].

1.2. Repair works and results

Repair operations are of considerable economic interest, especially for high added-value parts. In fact, the time, energy and material used in a repair is much lower than in the replacement case [9]. Nevertheless, the control of these operations is necessary (structure of the repaired material, heat affected zone (HAZ), etc.), in order to guarantee a good performance of the repaired part [10].

Additive manufacturing (AM) is a technology that is rapidly developing. It allows the creation of complex parts by adding successive layers of material [11]. The Laser Metal Deposition (LMD) process with powder is particularly adapted to the repair process in comparison with the welding process [12]. Indeed, the range of available powders is large.

Similarly, the process brings limited heat input to the substrate [13], and has excellent metallurgical continuity [14] and low dilution rates [15]. The use of various integrated equipment such as the computer numerical control (CNC) machine and a three-dimensional (3D) scanner makes it possible to have a high precision and to automate the repair process [16].

Zhang *et al.* [17] worked on volume optimization of the repair of a multitude of conical holes. But the optimization is performed on cross sections of the defects using a U-shaped profile. Furthermore, no repair trials have been performed and do not provide any evidence of the viability of this volume optimization for repair.

On the other hand, practical repair tests have been carried out with the LMD process. For example, Yu *et al.* [12] show the feasibility of this process for the repair of grooves in cast iron compared to welding, which is more damaging for the repaired parts. The studies on groove repair are extensive and do not attempt to optimize the repair volume [18–21] . Another study by Liu *et al.* [22] develops new deposition pattern for hole-type defect repair, but still using a unique geometry. Less academic works present the repair of high value-added parts such as the work of Koehler *et al.* [23] on the repair of damaged crankshafts of marine diesel engines, or the work of Wilson *et al.* [24] on the repair of turbine blades. Other studies are also working on the repair/recharging of railroad rails with the LMD process, such as the study by Lai *et al.* [25].

The studies cited above focus on adding material to flat and open surfaces or simple geometries of confined pre-machining such as grooves. Consequently, these solutions do not optimize the repair volume and repair of fine and deep defects such as corrosion pits. In addition, in the previous mentioned works, they do not take into account the influence of the deposition pattern and the surface condition of the substrate, which could have an impact on the quality of the repair.

1.3. Objectives

The objective of this paper is to present a strategy to repair damaged metal parts by pitting corrosion. The first step of the process is to identify the surface defect and to pre-machine the damaged surface in the form of an ellipsoid. The pre-machining in ellipsoidal shape will allow removing the defect and surface contaminants by machining the least material possible and to give a good accessibility to the projection nozzle. This step is essential in the study and requires a numeric optimization section. In fact, it consists in minimizing the volume to be repaired for fine and deep defects, while making the bottom of the pre-machining accessible. Thereafter, the deposition step by AM refills the previously machined material. Existing deposition pattern will be adapted to this pre-machining geometry, not previously studied in the literature. In addition, two surface states will be used to observe their influence on the repair. The characterizations carried out at the end of the process will make it possible to indicate the final quality of the repairs. The difficulty of the work is both on the theoretical and experimental part.

The content of this paper is organized as follows: section 2 defines the numerical chain allowing the automation of the repair process. Section 3 presents the optimization of the repair volume geometry. Section 4 shows the experimental repair of an optimized pre-machined geometry with LMD process. Section 5 discusses the experimental results and the main highlights. Finally, section 6 proposes conclusions to this study.

2. Overview of the numerical chain

With AM, it is possible to completely automate the parts reparation. It can be considered a numerical chain that allows, from a part that contains a pitting corrosion defect,

to acquire the shape of the defect, the construction and optimization of the repair volume, the machining and repair of the defect, as explained Kanishka *et al.* [26] in their paper.

2.1.Acquisition

In the case of a corroded part, the first step is to remove the corrosion products using the methods described in ASTM G01-03 [27]. Depending on the material and the degree of corrosion, cleaning can be mechanical, chemical or electrolytic. The first step of this numerical chain is the scan of the surface of the corroded part in order to have its dimensions, using a surface topography, 3D scan or coordinate measuring machine [16]. In addition, it is possible to reconstruct the surface of the part without the defect in order to have the repair volume. After processing the point cloud obtained by the measurement, it is possible to make the segmentation to isolate the defect [28]. In general, the acquisition allows having the upper and lower surface of the repair volume.

Influential parameters during the acquisition of the part geometry can be the resolution of the chosen measurement, the calibration of the measuring device, the accessibility of the defect by the sensor, as well as the external environment such as temperature. The acquisition process needs to be developed, as there is no automatic method to date.

2.2.Repair volume construction

After acquiring the shape of the defect and its dimensions, the repair volume must be digitally modeled in order to perform the machining and filling in a digital manner. This step consists in building an envelope to represent the repair volume from an optimization of the ellipsoid parameters. The envelope consists of two surfaces, an upper surface that represents the surface of the part where the defect is located, and a lower surface that represents the defect to be repaired. In this study, the optimization minimizes the repair volume from a

parallelepiped-shaped bounding box of the defect, as presented in Figure 2 and satisfies the imposed constraints (*i.e.* geometrical and technical constraints). The section 3 details the construction of this repair volume and its optimization.

The convergence of the optimization to the most optimal result depends on factors, which are the size of the surfaces discretization in the program, and the numerical resolution.

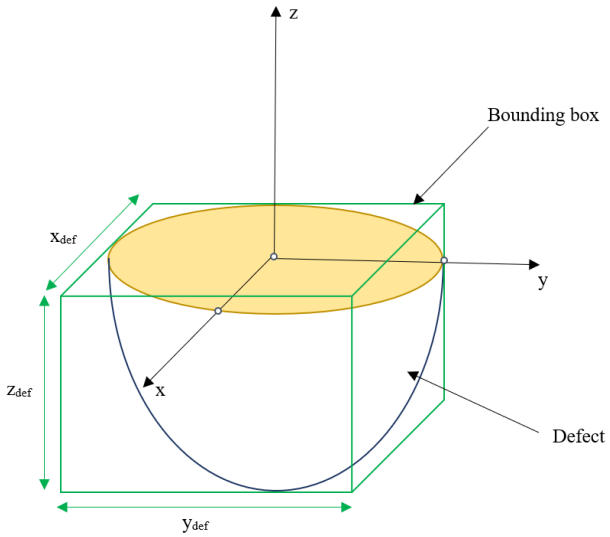

Figure 2. Representation of the defect and its bounding box.

2.3.Machining

The purpose of machining is to remove the defect and to have a regular shape to make the material deposition. It is possible to control the surface finish by choosing the parameters of the machining (*e.g.*, feed rate, depth of cut ...) appropriate to the material and the machining tool [29,30]. The defects studied in this work have ellipsoidal shape, and in this case, milling is best suited to machine this geometry using a ball end mill.

In machining, the surface finish is dependent on the ridge height and the machining tolerance, which can be determined from the tool radius, the radius of curvature of the machined surface and the transverse and longitudinal step of the machining path. The scallop height is influenced more by the transverse step, while the machining tolerance is influenced by the longitudinal step [31], as illustrated in Figure 3.

$$h_c = f(r, R_t, P_t) \quad (1)$$

$$T_u = f(r, R_l, P_l) \quad (2)$$

Where h_c is the scallop height, T_u the tolerance machining, R_t the transverse curvature radius, R_l the longitudinal curvature radius, r the tool radius, P_l the longitudinal step and P_t the transversal step.

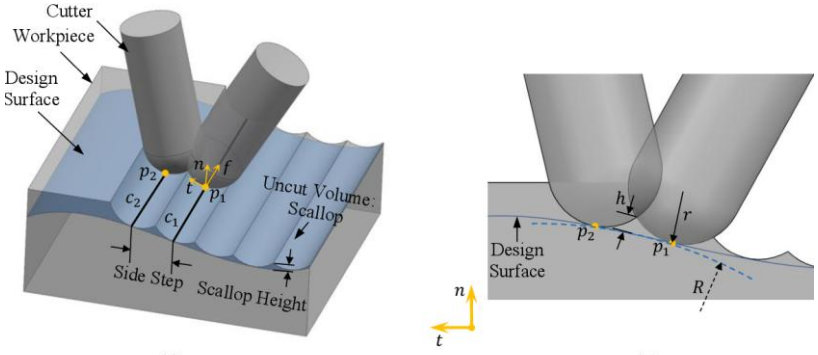

Figure 3. Illustration of scallop geometry and tool path parameters [31]

The authors Urbikain *et al.* [32] developed a model capable of predicting the surface roughness of a part machined with an end ball mill according to a combination of geometric and cutting parameters. In the same paper, they demonstrated that the angle between the part and the tool has a strong influence on the roughness of the machining and this must be taken into account in the repair volume optimization algorithm.

The pre-machined shape must respect the technical constraints of machining, among others, the minimum radius of curvature of the ellipsoid, which must be smaller than the radius of the tool used so that there is no interference (overcut) with the part. In addition, the shape of the pre-machining must also respect geometrical constraints such as the depth and the opening angle to allow the deposition by AM. These elements are detailed in the section 3.

2.4.Filling

The last step of this digital chain is the filling of the repair volume using AM to deposit the material in the pre-machined shape in the previous step. The quality of the deposition

depends on a large number of machine parameters, such as the power of the laser, the speed of the deposition nozzle or the powder feed rate [33]. In addition, the quality of the raw materials can influence the quality of the repair, depending on the particle size of the powder or the surface condition of the substrate [34].

In a previous study [35], a parametric optimization of the main machine parameters (laser power, nozzle speed, powder feed rate) resulted in a dense, crack-free deposit with minimum porosity. These parameters were optimized in order to obtain a metallurgical continuity between the substrate and the deposit, as well as between the layers for groove-type defects. However, the ellipsoidal geometry of this study requires adapting the deposition strategies, in order to avoid the formation of porosity, in particular lack of fusion with the edges of the substrate, which can lead to a poor metallurgical bonding. In fact, the literature show the effect of the tilt angle between the surface and the projection nozzle, which can affect the geometry of the melt pool [36].

After depositing the material, a finishing post-machining is necessary to remove the excess material. The curved shape of the beads requires the addition of an extra layer to completely fill the pre-machining.

3. Optimization of the repair volume geometry

In order to carry out the repair operations (machining and filling) of a part, it is first necessary to identify the repair volume. This volume is included between an upper surface, which is the surface of the part without defect, and a lower surface, which represents the shape of the defect to be repaired.

The optimization of the ellipsoid consists in finding the ideal dimensions and the position of the center to minimize the repair volume, while respecting the various constraints related to machining and filling.

3.1.Modeling of the different geometric elements

NURBS tiles model the upper surface of the part to be repaired. A STEP file created with CATIA generates the surface, as presented Figure 4 (a). The NURBS surface is a parametric model, which has the following form:

$$S_{up}(u,v) = \sum_{i=0}^{n}\sum_{j=0}^{m} {B_i}^n(u)\ {B_j}^m(v)\ P_{i,j} \tag{3}$$

where B_i is the basic function and $P_{i,j}$ the control point.

The lower surface represents the surface of the defect, which is an ellipsoidal surface modelling with parametric equations. The ellipsoid is defined by its dimensions a, b and c, as presented in Figure 4 (b), which represent the half axis lengths along the three directions of space, as well as the position of its center in space. The equation of an ellipsoid can be expressed in the following form:

$$\frac{x^2}{a^2}+\frac{y^2}{b^2}+\frac{z^2}{c^2}=1 \tag{4}$$

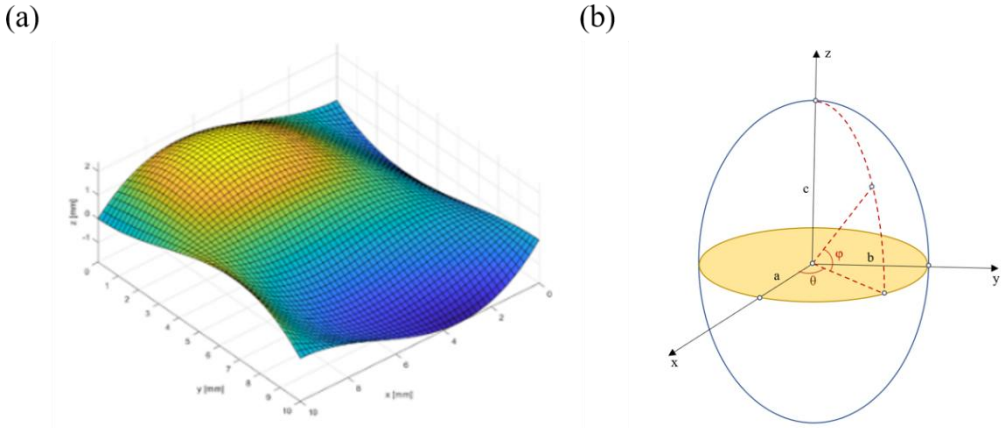

Figure 4. (a) Matlab upper surface model and (b) parameters of an ellipsoid.

On the other hand, it is possible to parameterize an ellipsoidal surface using the following equations:

$$S_{ellipsoide}(\theta,\varphi)=\begin{cases}x=a\cos(\theta)\cos(\varphi)\\ y=b\sin(\theta)\cos(\varphi)\\ z=c\sin(\varphi)\end{cases} \quad (5)$$

where $\theta \in [0,2\pi]$ and $\varphi \in \left[-\frac{\pi}{2},\frac{\pi}{2}\right]$

In order to parameterize the ellipsoid in u and v, the following change of variables are made:

$$\begin{cases}\theta=2\pi\, u\\ \varphi=\pi\left(v-\frac{1}{2}\right)\end{cases} \quad (u,v) \in [0,1]^2 \quad (6)$$

The following equations are obtained:

$$S_{ellipsoide}=\begin{cases}x=-a\cos(u)\sin(v)\\ y=-b\sin(u)\sin(v)\\ z=c\cos(v)\end{cases} \quad (7)$$

The position of the center of this ellipsoid is determined by the position of the defect on the upper surface. It is assumed that the defect is in the middle of the upper surface. The vector $\vec{z}$ is noted as the position of the center of the ellipsoid with following a reference frame.

In order to determine the intersection between the upper surface and the ellipsoidal surface such that $S_{up} \cap S_{ellipsoid} = C_{intersection}$, the parameters u and v must respect for each surface the following equation:

$$S_{up}(u_{up},v_{up}) = S_{ellipsoide}(u_{elps},v_{elps}) \quad (8)$$

Where S_{up} is the upper surface, $S_{ellipsoide}$ the ellipsoid surface, u_{up} the radial unit vector and v_{up} orthoradial unit vector of the upper surface and u_{elps} the radial unit vector and v_{elps} orthoradial unit vector of the ellipsoidal surface.

A numerical resolution is chosen, in order to select all the points of the ellipsoid closest to the upper surface. This part is realized by calculating the distance between the points of the ellipsoid and the points of the upper surface. Then a reference distance is chosen to select the points of the corresponding ellipsoid, which allows having the intersection points, as observed Figure 5.

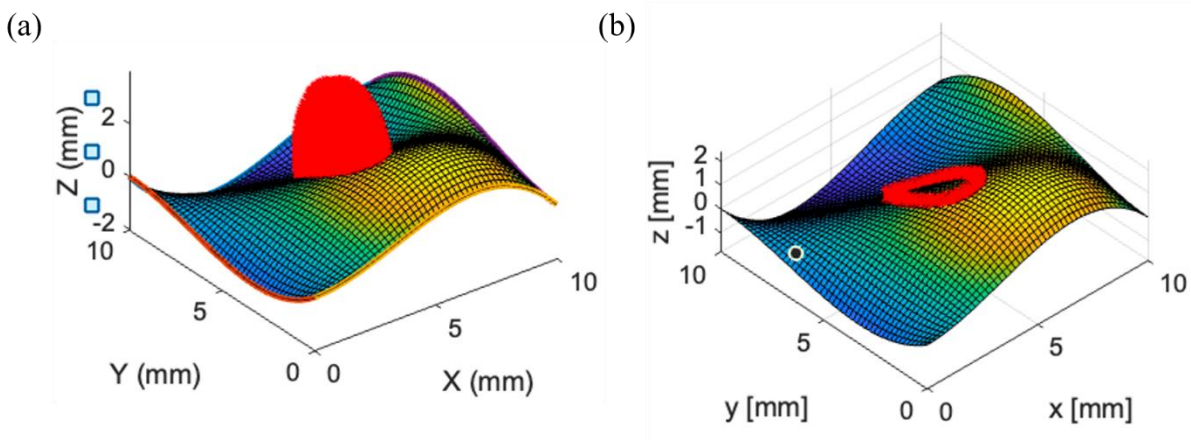

Figure 5. Intersection of surfaces (a) positioning of the ellipsoidal surface in the upper surface, (b) intersection points between the ellipsoidal surface and the upper surface.

The lower surface is the surface of the ellipsoid below the upper surface. Such as:

$$S_{low}(u,v) = S_{ellipsoide}(u_{low}, v_{low}) \,|\, S_{ellipsoide}(u_{low}, v_{low}).\mathbf{k} \leq S_{up}(u,v).\mathbf{k} \qquad (9)$$

with $\mathbf{k}=\begin{cases}0\\0\\1\end{cases}$

In the numerical approach, it is possible to generate the bottom surface by deleting the points that are above the intersection points. Depending on how the ellipsoid is parameterized, the points above the intersection can be removed line by line. At the end of the processing, only the lower surface will remain, as highlighted in Figure 6.

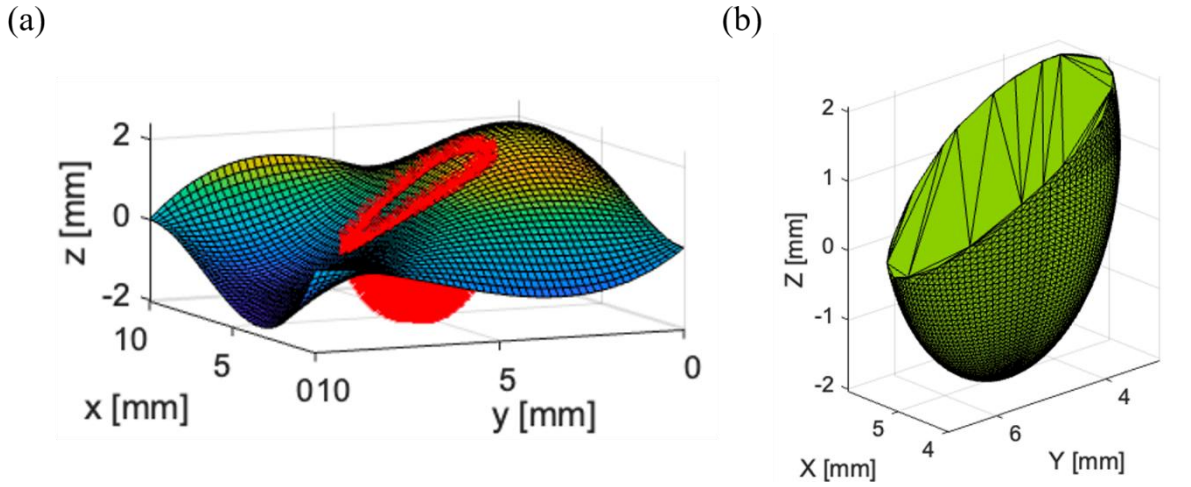

Figure 6. Lower surface (a) point removal and (b) repair volume.

3.2.Definition of the function and constraints

3.2.1. **Dimensional constraints**

The dimensions of the ellipsoid at the intersection and the depth must encompass the defect. This constraint leads to writing the following inequalities:

$$\begin{cases} ix \geq x_{def} \\ iy \geq y_{def} \\ iz \geq z_{def} \end{cases} \quad (10)$$

where ix, iy and iz are the dimensions of the repair volume.

For accessibility reasons of the nozzle during the filling process, it must be ensured that the maximum depth of the bottom surface does not exceed a specific depth determined according to the nozzle used.

$$iz \leq \max depth \quad (11)$$

The values of ix and iy are determined from the intersection points, iz can be calculated from the following expression:

$$iz = c - dz \quad (12)$$

3.2.2. **Curvature constraints**

In order to machine the shape, it is necessary to ensure that the minimum curvature radius of the bottom surface is greater than the radius of the machining tool (here a hemispherical tool).

$$r_{min} \geq R_{outil} \quad (13)$$

To calculate the minimum radius of curvature, it is first necessary to calculate the maximum curvature of the surface, which is calculated from the Gaussian curvature and the mean curvature. According to the formula developed by Sebahattin Bektas [37], these curvatures can be calculated from the dimensions of the ellipsoid and the Cartesian coordinates of each point (Eq 14 and 15).

$$k_{Gauss} = \frac{1}{\left(a\ b\ c\left(\frac{x^2}{a^4} + \frac{y^2}{b^4} + \frac{z^2}{c^4}\right)\right)^2} \tag{14}$$

$$k_{moy} = \frac{x^2 + y^2 + z^2 - a^2 - b^2 - c^2}{2\ (a\ b\ c)^2 \left(\frac{x^2}{a^4} + \frac{y^2}{b^4} + \frac{z^2}{c^4}\right)^{3/2}} \tag{15}$$

The maximum curvature is obtained using the following equation:

$$k_{max} = k_{moy} + \sqrt{k_{moy}^2 - k_{Gauss}} \tag{16}$$

And so, the minimum radius of curvature is calculated using the following formula:

$$r_{min} = \frac{1}{k_{max}} \tag{17}$$

3.2.3. **Constraint on the opening angle**

For a better metallurgical bonding between the substrate and the deposit, it is necessary to have an opening angle α greater than a certain angle. At the intersection, the opening angles are variable depending on the position of the ellipsoid. Thus, the smallest calculated value will be used. (Eq.18).

$$\alpha_{min} \geq minimum\ opening\ angle \tag{18}$$

This opening angle is calculated at the intersection between the upper and lower surface of the repair volume, by calculating the angle between the tangent vector along the v-direction (Sv) at the intersection points and the vector n ($\alpha = \widehat{S_v\ n}$), as described in Figure 7.

$$\alpha = \arccos \frac{S_v\ .\ n}{\|S_v\|\ \|n\|} \tag{19}$$

With:

$$S_v = \frac{\partial S_{ellipsoide}(u, v)}{\partial v}$$

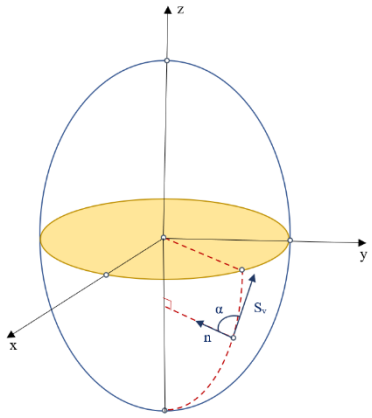

Figure 7. Opening angle represented at the intersection between the upper and lower surface

3.2.4. Objective function

The volume of repair aims to be minimized, in order to reduce the manufacturing time, as well as the material used. Analytically, it is difficult to calculate the repair volume, especially for complex upper surfaces (Eq. 20). However, it is possible to do it numerically by creating a mesh, which allows the calculation of the repair volume for any upper surface.

$$V = \int_0^a \int_0^p \int_0^q dx\, dy\, dz \tag{20}$$

With:

$$p = b\sqrt{1 - \frac{x^2}{a^2}} \;\; and \;\; q = c\sqrt{1 - \frac{x^2}{a^2} - \frac{y^2}{b^2}}$$

3.3. Implementation and optimization example

The algorithm developed in this work and shown in Figure 8 generates the repair volume and optimizes it. Based on the dimensions and position of the center of the ellipsoidal defect and the STEP file representing the upper surface, the program generates the lower surface by deleting the points of the ellipsoid, which is located above the upper surface. The next step is to optimize the parameters of the ellipsoid from the initial solution by calculating at each iteration the optimization function, which is the repair volume. At any time, the algorithm respects the following constraints: the initial solution has dimensions greater than

317 those of the defect, the opening angle must be greater than a minimum, the minimum
318 curvature must be greater than the curvature of the tool, and the final solution must lie within
319 the bounding box of the repair volume.

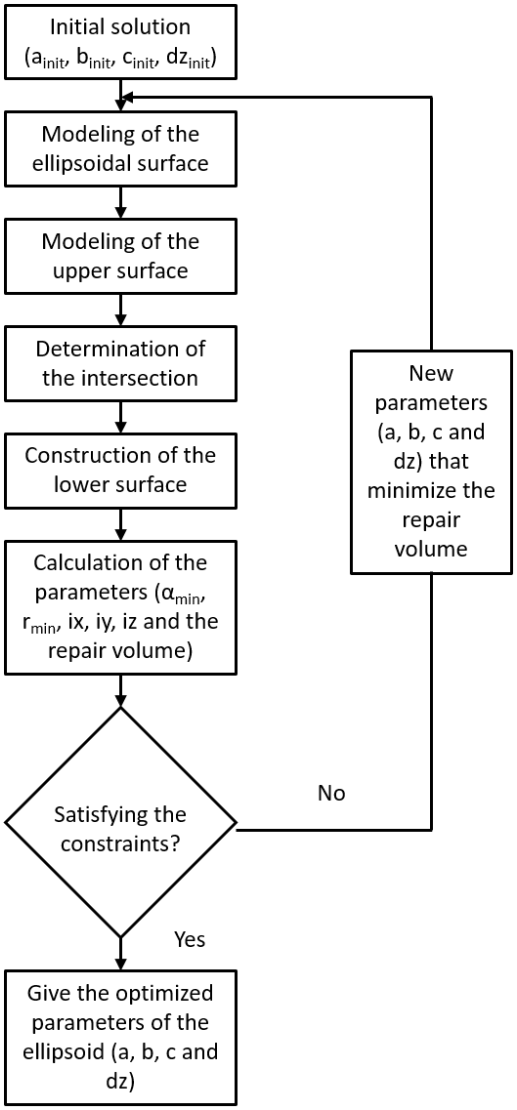

320

321 **Figure 8.** Algorithm for the ellipsoid parameters optimization.
322
323 To validate the correct operation of the developed program, the case of a defect on a flat
324 surface is tested. The values of the chosen parameters are summarized in Table 1.

325 **Table 1.** Input parameters.

Parameters	Values
Defect dimensions	x_{def} = 8 mm y_{def} = 12 mm z_{def} = 4 mm dz = 0 mm
Initial solution	a_{init} = 6 mm

	b_{init} = 8 mm c_{init} = 6 mm dz = 0 mm
Milling tool radius	R_{tool} = 3 mm
Opening angle	α = 120°

The calculation time is about 200 seconds. The optimization results in an ellipsoid that respects all the imposed constraints. This ellipsoid of dimensions $10 \times 14 \times 25\, mm^3$ with an offset of the center dz = 20 mm, which allows to obtain a hole of dimensions $10.5 \times 15.75 \times 5\, mm^3$, as presented in Figure 9.

4. Application of the optimized repair volume in a case study

Repair tests of ellipsoids pre-machined in a SS316L substrate are carried out in order to validate the previous numerical chain, as well as the feasibility of repairing pre-machined parts of complex shape with the LMD process. The difficulty of this work lies in the confinement of the defect, despite the constraints on the opening angle, as well as the adaptation of the scanning strategies to this shape and the rounded surface, which tends to destabilize the melt pool. Thus, two deposition pattern will be adapted, namely the zigzag and contour strategies, and the influence of the surface condition between a sandblasted and non-sandblasted surface will be observed.

4.1.Raw materials

The raw materials used in this study are a SS316L plate of dimensions 250x100x20 mm^3, as a support for the repairs and a SS316L powder (supplied by ERASTEEL, Sweden) of granulometry 45-106 µm, as filler metal. The compositions of the two elements are given by the manufacturers in the Table 2 and comply with the ASTM A276 standard [38].

Table 2. Chemical composition of SS316L powder and substrate compared to ASTM specifications (wt %).

Element	Fe	Cr	Ni	Mn	Mo	C	P	Si	S
Powder	Bal.	17.6	13.6	1.67	2.69	<0.02	0.007	0.54	0.006

Substrate	Bal.	16.63	10.03	1.33	2.02	0.017	0.029	0.421	0.001
ASTM A276	Bal.	16-18	10-14	2.0 Max	2-3	0.03 Max	0.045 Max	0.75 Max	0.03 Max

4.2.Pre-machined ellipsoid

A 3-axis CNC milling machine (DMG HSC 75V) is used for the machining of ellipsoids in the substrate, as presented Figure 9. The optimized dimensions of the ellipsoid presented previously are used for the experimental repair. The machining paths were generated by CATIA from a computer-aided design model of the plate to be realized. The machining was done with a hemispherical tool in monobloc carbide with a diameter of 6 mm. Concerning the cutting conditions, the chosen feed rate is 180 mm/min and the spindle speed is 3700 rpm with a depth of cut of 0.5 mm.

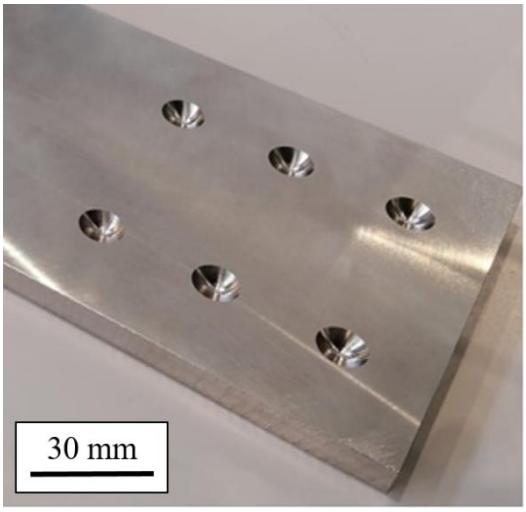

Figure 9. Ellipsoidal holes machined in the SS316L substrate.

Naesstroem *et al.* [39] demonstrated that LMD deposition on different surface conditions affect slightly the quality of the deposits. However, these tests were performed on unconfined flat surfaces. It is interesting to observe whether two surface conditions can affect the quality of the repair. Half of the pre-machines were sandblasted, in order to observe the influence of sandblasting on the final quality of the repair. Table 3 shows the surface condition of the machined and sandblasted holes obtained by surface topography. A smoothing of the surface after the sandblast is noticed.

Table 3. Surface roughness of the ellipsoidal holes according to ISO 25178-2 [40].

	Sa (mm)	Sz (mm)	Ssk	Sku
Surface without sandblast	0.34	1.71	0.72	2.33
Sandblasted surface	0.3	1.68	0.3	2.28

4.3.Filling the missing material

A 3-axis LENS MR-7 System machine (OPTOMEC, Inc. Albuquerque, NM, USA) is used to represent the LMD process with powder, illustrated in Figure 10 (a). In order to limit oxidation, the chamber is under a controlled environment with ultra-pure argon. A melt pool is created with an YLS-3000-CT laser, and at the same time supplied with powder from a coaxial nozzle. The movement of the projection head makes the cords in all directions of the space. The deposition parameters used are a laser power of 650 W, a nozzle speed of 10 mm/s, a powder feed rate of 6.6 g/min and a hatching distance of 0.84 mm. This configuration results in a bead of 1.2 mm wide by 0.5 mm effective height, with a dilution of 30% between each layer.

The deposition pattern were automatically generated by ESPRIT software and converted into G-code program. The first strategy is the zigzag filling, which consists of making a zigzag path for each layer starting with a contour bead and the second is the contour filling which starts with the outer contours and moves inwards, as highlighted Figure 10 (b) and (c).

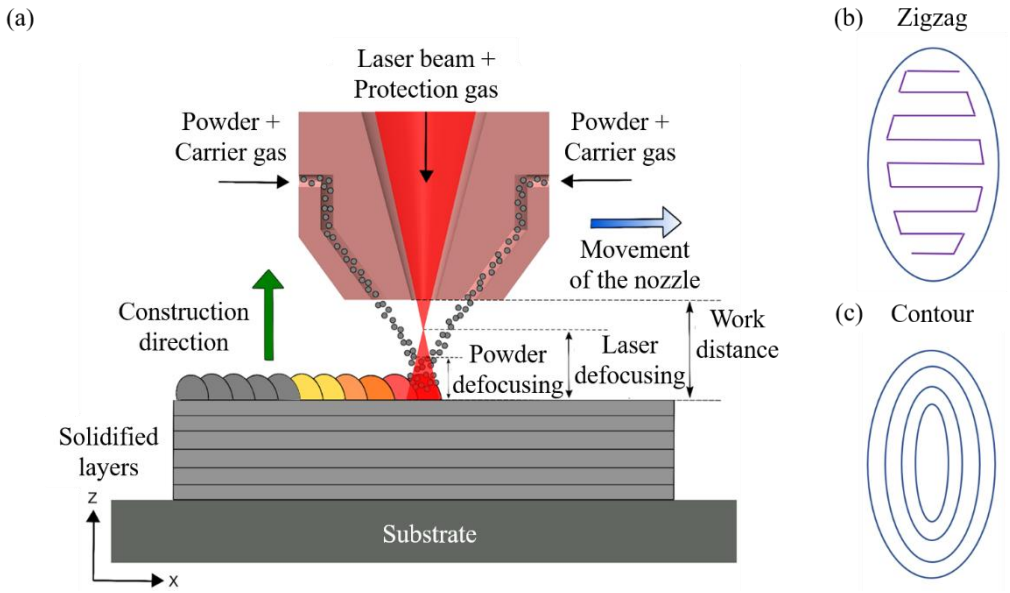

Figure 10. Principle of (a) LMD process with powder, (b) zigzag strategy and (c) contour strategy.

4.4.Characterizations

The density of the samples is observed by image analysis of the mirror polished cross section. The Archimedean method is not suitable for the case of repairs, as it essentially measures the density of the substrate, which is the major part of the sample.

An oxalic acid (10%wt) electropolishing highlights the two elements of our repair, as shown in Figure 11, with the deposit in the center in black and the substrate on the outside in white.

The presence of intra-layer porosities, especially spherical ones, is observed in the samples, as presented in Figure 11. They are the result of the vaporization of some elements of the melt pool, which lead to the imprisonment of gas in the solidified bead [41]. A minor optimization of the process parameters would reduce their number, but is not the purpose of this work.

Inter-layer porosities are also present in the repaired samples. In contrast to the intra-layer porosities, they have a constant position depending on the deposition pattern, independently of the surface condition of the material. They are recognizable by their

404 irregular shape and can be generated by wrong process parameters (*e.g.*, too low power),
405 wrong adaptation of the pattern deposition, or influenced by the chamber atmosphere [42].

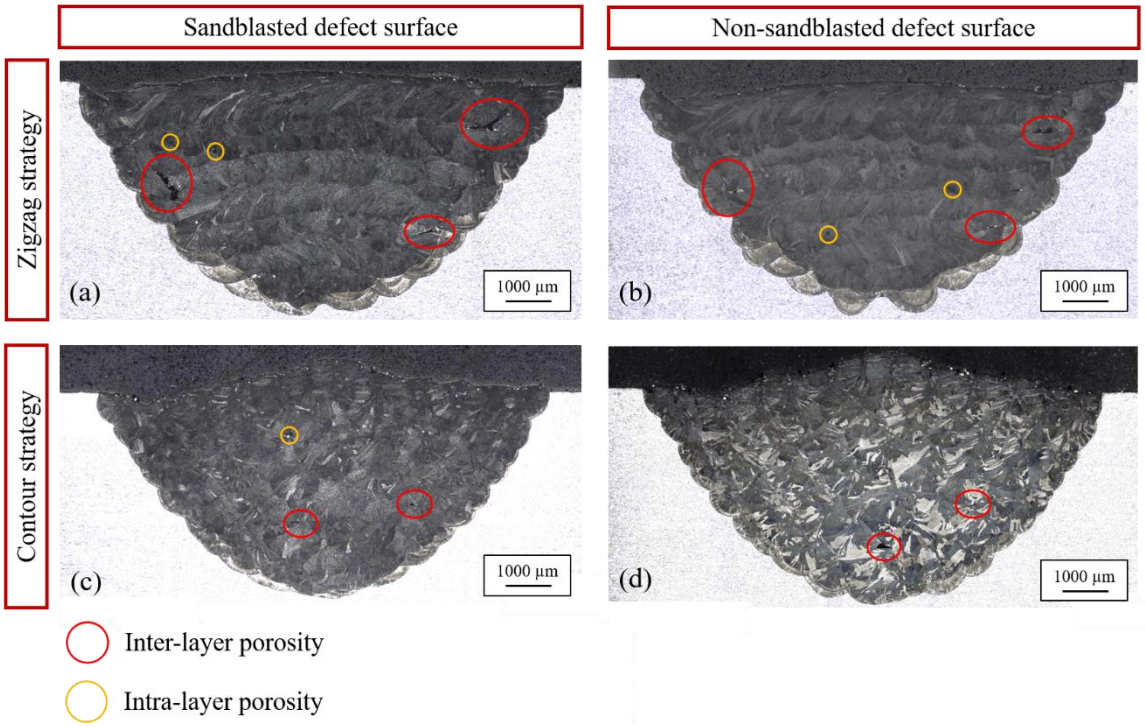

406

407 **Figure 11.** Cross-sections of the repaired samples: (a) blasted – zigzag, (b) non-blasted –
408 zigzag, (c) blasted – contour and (d) non-blasted – contour.
409
410 EBSD mapping was performed to determine the grains size and morphology. The
411 results highlight a heterogeneous microstructure of the repair, with the presence of three
412 distinct zones (*i.e.*, the deposit, the HAZ and the substrate).

413 The deposit is characterized by a coarse and columnar microstructure with preferential
414 growth axes and an austenite FCC structure, as characterized in the deposit of the repair in
415 Figure 12 and in Figure 13 (a). During the solidification of the bead, a strong thermal gradient
416 is present in the melt pool, generating a growth of the grains in the direction of the thermal
417 gradient, *i.e.* towards the middle of the melt pool and in the direction of displacement of the
418 projection nozzle, as observed in Figure 12 (a) [43]. Figure 12 (a) and (b) highlight the
419 cellular substructure, which is formed in the grains of the deposit due to the very fast cooling
420 of the melt pool of the order of 10^4 K/s and is characteristic of the LMD process. A high

density of dislocations is formed as a result of solidification due to the heterogeneities of heating and cooling during LMD process and assemble into cellular patterns at cell boundaries [44]. This substructure is the segregation of the stainless steel elements. The center of the cells is rich in iron, while the edges are rich in alloying elements such as Cr, Ni, Mn and Mo [43,45]. Also, a remelting between the layers of 30% is performed, in order to allow an epitaxial growth favoring the metallurgical continuity. The Figure 13 (b) and (c) highlight the epitaxial growth of grains between the substrate and the deposit and between the different layers. This phenomenon contributes to a strong metallurgical bonding throughout the repair. It should be noted that this epitaxial growth results in smaller grains in the beads in contact with the substrate than in the rest of the deposit.

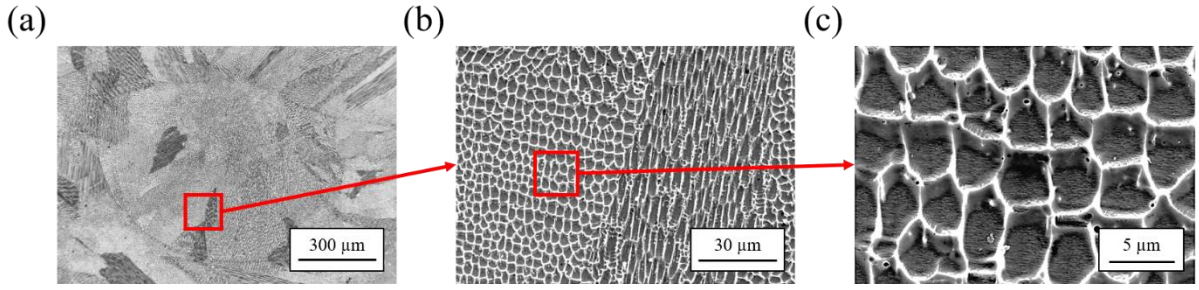

Figure 12. SEM observations: (a) solidified melt pool, (b) columnar grains and (c) cellular substructure

The HAZ and the substrate have a similar microstructure, which is fine and equiaxed as presented in Figure 13. In fact, the substrate has a classical microstructure of a stainless steel produced in steel mills, having been manufactured in continuous casting, hot rolled and with the application of a post heat treatment at 1050°C. It is mainly composed of an austenite phase, but presents some small grains of residual ferrite, which did not disappear during the heat treatment. The proportion of ferrite in the substrate is about 0.5 %. On the other hand, the HAZ presents slightly larger grains than in the substrate, while remaining equiaxed and with a higher proportion of ferrite in the order of 2.4 %. The HAZ is the substrate closest to the

deposit that has not received enough energy from the laser to melt, but enough energy to undergo local recrystallization with phase changes, followed by a very rapid cooling [46].

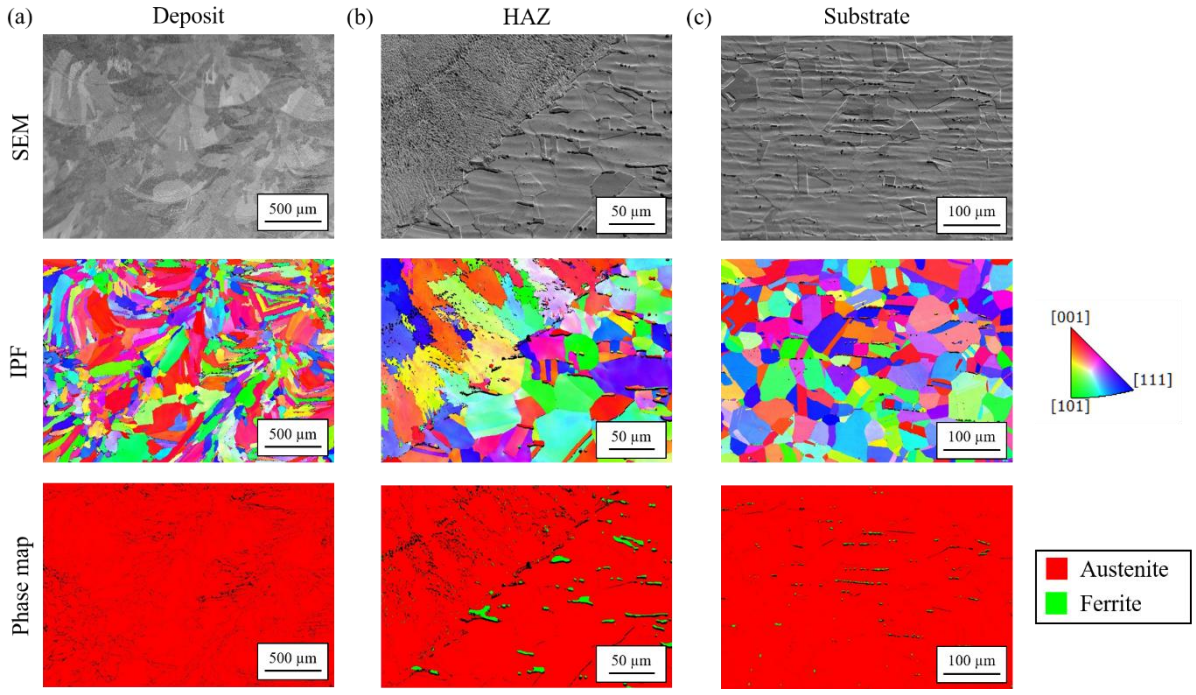

Figure 13. SEM observations, IPF and phase map: (a) substrate, (b) HAZ and (c) deposit

Figure 14, which results from EBSD mapping, highlights that the deposition pattern or the surface condition has no influence on the grain size in the three studied areas (*i.e.*, the low interface, the left interface and the center of the deposit). Indeed, the distribution curves generated from the histograms are similar. Their variations are due to the number of grains counted on each EBSD map, which depends on the area analyzed. Furthermore, as shown in Table 4, it is observed that regardless of the method used, the difference between the volume-weighted average grain sizes is insignificant, indicating invariability of grain size depending on the method used for pre-machining repair. On the other hand, it is observed the significant increase of the grain size between the substrate, the interface and the deposit. In fact, the grain size is doubled or even tripled between the substrate and the interface, and quadrupled between the substrate and the deposit, with much higher standard deviations in the deposit.

This means that in addition to a much larger grain size, the deposit has a more variable microstructure than in the substrate.

This observation highlights the heterogeneity of the microstructure due to processes with different kinetics.

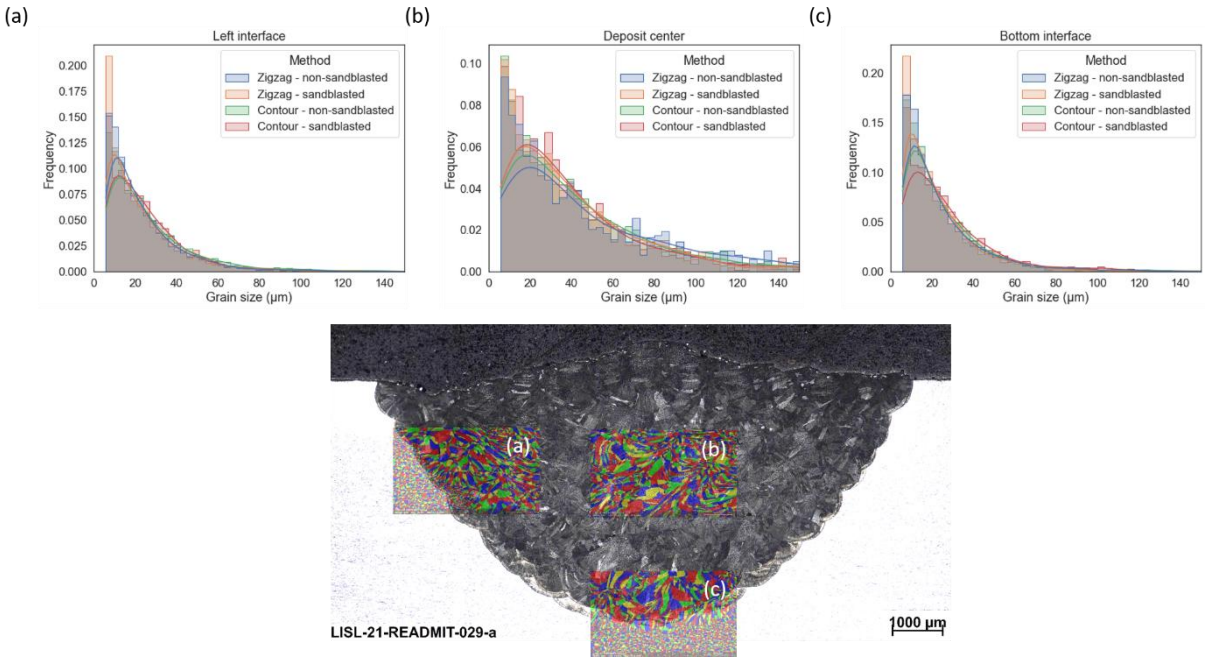

Figure 14. Grain size distribution in three zone of the repair: (a) left interface, (b) deposit center and (c) bottom interface

Table 4: Statistical values of the volume-weighted average grain size of each method for the areas studied

Method	Substrate (µm)		Left interface (µm)		Deposit center (µm)		Bottom interface (µm)	
	volume-weighted average	std	volume-weighted average	std	volume-weighted average	std	volume-weighted average	std
Contour - non-sandblasted	35.2	15.7	92.5	64.1	128.6	72.6	109.1	92.7
Contour - sandblasted			76.6	57.6	130.9	82.5	93.5	73.5
Zigzag - non-sandblasted			85.6	69.9	146.6	82.8	93.3	71.2
Zigzag - sandblasted			75.4	58.4	116.1	70.4	64.5	48.5

Microhardness tester (STRUERS Durascan70, Vickers) with a load of 5 kg was used to perform microhardness mapping on the cross sections to observe the influence of the parameters on the mechanical properties of the repaired parts, as presented in Figure 15. A hardness gradient can be observed in the repair, especially for the zigzag repair. Indeed, the

substrate has a hardness of ~160 HV and the HAZ and the near deposit a hardness of ~200 HV. The microhardness value in the deposit varies from 180 HV to 250 HV. The surface condition of the pre-machining did not seem to have any influence on the hardness of the samples. However, a difference in hardness is observed depending on the use of the deposition pattern.

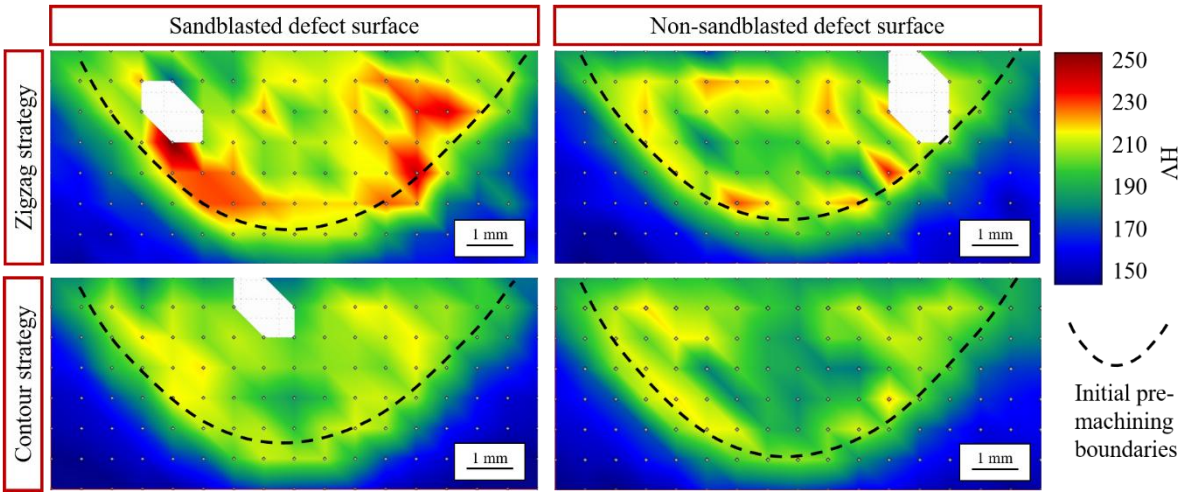

Figure 15. Microhardness mapping of the repaired specimens: (a) blasted – zigzag, (b) non-blasted – zigzag, (c) blasted – contour and (d) non-blasted – contour.

5. Discussion of the results

The presence of porosities in the zigzag pattern is induced by an error in the calculation of the number of beads per layer. Indeed, in each layer of this strategy, a contour bead is made on the surface of the pre-machining, then a zigzag filling is made inside this contour bead. The number of parallel beads is calculated by dividing the width to be filled by the hatching distance. However, arriving at an integer number is rare and the number of beads to be deposited is approximated to the nearest integer. Thus, in the case of the study, each layer is missing a bead, which explains this porosity due to a lack of material.

For the contour deposition strategy, beads with the shape of ellipses are deposited starting from the outside and ending with the centermost bead. Porosities are present on the first layers. The most likely hypothesis explaining these porosities is that with a fixed

hatching distance, the space left for the last bead to be deposited is too small for it to penetrate the material and form a lack of fusion.

For the two deposition pattern, the inter-layer porosity formation is due to the confinement of the material deposition in a pre-machining. It is necessary that each bead has its location in the pre-machining to avoid porosity formation. One solution would be to adapt the hatching distance to each layer. Thus, each bead would have sufficient space to be deposited without being disturbed by the other beads.

Deposition pattern and surface conditions do not affect grain size at the interface or center of the deposit. All four conditions show comparable grain size distribution curves. The only difference observed is between grains counted at the interfaces and at the center. The average grain size of the interfaces is smaller than at the center. This is because at the interfaces, the fine and equiaxed grains of the substrate are counted. Also, it is observed that the grains of the beads in contact with the substrate are finer than those in the center. This phenomenon is related to the epitaxial growth of the bead grains on the substrate grains during solidification. Indeed, the grains of the substrate are fine compared to those of the deposit made by LMD. But when the melt pool of the bead starts to solidify, its grains grow epitaxially on the substrate grains in contact, creating a multitude of fine and columnar grains at the interface. This effect disappears afterwards, because the grains solidifying last in the melt pool have already grown enough that the grains of the next bead have only a few coarse grains left on which to grow. A similar observation is made in the work of Balit *et al.* [47], who show two regimes of grain growth in the deposit, the first in the beads in contact with the substrate, then in the rest of the deposit.

As previously explained, the substrate has a microhardness of about 160 HV, which is in accordance with the values given by the manufacturer. However, the HAZ has a higher hardness than the substrate. This increase in hardness can be explained by the formation of

delta ferrite in the HAZ, which has a higher plasticity than austenite and causes an increase in hardness [48,49]. Also, the successive deposition of the beads leads to heating and cooling cycles which introduce residual compressive stresses and tend to increase the hardness value, through the presence of a high density of dislocations [50]. Finally, the in-depth hardening of an austenitic stainless steel by the passage of a laser beam at low speed is demonstrated in the work of Martinez *et al.* [51]. In fact, this process is also used by other techniques for surface hardening of a steel by the introduction of compressive residual stresses. In the case of the study, the passage of the laser is done at low speed

The microhardness of the deposit is variable. In fact, it is observed that the microhardness in the beads in contact with the substrate is higher than in the rest of the deposit. This phenomenon is related to the fineness of the grains of the beads in contact with the substrate, caused by the epitaxial growth of the grains from those of the substrate, as explained previously. Thus, according to the Hall-Petch relation, the microhardness is higher at the edges than in the center of the deposit. This result is observed regardless of the deposition strategy and the surface condition of the pre-machining.

Moreover, the deposit has a higher hardness than the substrate. Nevertheless, the grains have a larger size. According to the *Hall-Petch* relation, the microhardness should be lower. However, the microstructure of the deposit is particular, since it is multi-scale and is composed of solidified melt pool, grains and a cellular substructure. These elements are obstacles to the diffusion of dislocations. Zhou *et al.* [52] demonstrated that the strengthening mechanism of SS316L parts made in SLM is the combination of these elements. Thus, the Hall-Petch relationship is strongly influenced by the cellular substructure, which has a high dislocation density. This hinders the movement of dislocations and leads to a higher hardness. This may explain the difference in intensity between the Zigzag and Contour strategies. In fact, the Contour strategy deposits the bead next to the previous bead while it is still hot,

resulting in a coarser cell substructure and thus a lower microhardness. In contrast, the Zigzag strategy starts laying down the beads on one side of the pre-machining and finishes on the other, allowing more time for the contour bead to cool, resulting in thinner cells and thus higher microhardness.

An unverified hypothesis in this paper is that the variation of the Vickers microhardness in the deposit is due to the elastic return after indentation. It is characteristic of an anisotropic material and is more or less pronounced depending on the orientation of the indented grains. In addition, the state of the residual stresses present in the material can strongly vary this measurement. Tsui *et al.* proved that the load applied to a part varies the measured microhardness, especially the tensile stresses [53]. Thus, the variation of microhardness in the deposit represents the residual stress state present. Unfortunately, without knowing the value of microhardness without stresses, it is complicated to know if they are tensile or compressive residual stresses and even less their values. However, it is noticed that the microhardness is more homogeneous with the contour strategy. While the Zigzag strategy shows a large variation of microhardness in the deposit, with peaks in the areas where the Zigzag path beads and the contour bead meet. The abrupt change in direction between the beads appears to concentrate residual stresses. Thus, the contour strategy with some optimizations appears to be the most mechanically sound deposition pattern for ellipsoid repair.

6. Conclusion

In this work, elements of the numerical chain allowing the repair of elements damaged by pitting corrosion was developed. A numerical optimization of the repair volume in the shape of ellipsoids and experimental tests under different conditions were investigated. The main conclusions are summarized below.

The numerical optimization tool minimizes the repair volume to remove only the damaged material. The ellipsoidal surface, whose initial dimensions are taken from the corrosion pit, is generated at each iteration of the optimization. A surface below the nominal surface is generated, which creates the repair volume, while the geometric (i.e., initial defect size and opening angle) and technical (i.e., tool radius) constraints are respected in the repair volume optimization calculation.

Experimental tests demonstrate the feasibility of repairing ellipsoidal pre-machining using LMD. Sandblasting does not affect the final quality of the repair. However, adjusting the overlapping rate at each layer would avoid the formation of porosity in the deposit. The microstructure of the repair is heterogeneous with fine and equiaxed substrate grains and coarse and columnar deposit grains. An increase in microhardness in the HAZ and near the deposit is caused by the formation of a delta ferrite phase and smaller grains than in the rest of the deposit, respectively. Similarly, the variable microhardness intensity in the deposit is due to the cellular substructure influenced by the deposition pattern. The contour strategy shows a more homogeneous distribution of microhardness in the deposit.

In perspective, optimizing the repair volume in a different bounding box would result in a smaller ellipsoid. Seawater immersion tests and electrochemical polarization tests would allow to verify the corrosion resistance of the repair compared to the reference substrate. Finally, residual stress measurements would be interesting to understand the effects of the deposition pattern on the repair.

Acknowledgements

This work was supported financially by the French Alternative Energies and Atomic Energy Commission (CEA) and the Ecole Normale Supérieure de Paris-Saclay (ENS-PS). The authors want to acknowledge Michèle Brehier for the generation of the filling trajectories.

Declaration of Competing Interest

The authors declare that they have no known competing financial interests or personal relationships that could have appeared to influence the work reported in this paper.

Credit authorship contribution statement:

Bilel Si-Smail: Methodology, Validation, Software, Investigation, Data curation, Formal analysis, Writing – original draft. **Thomas Cailloux**: Methodology, Validation, Software, Investigation, Data curation, Formal analysis, Writing – original draft, Writing – review & editing, Visualization. **Yann Quinsat**: Conceptualization, Methodology, Supervision, Writing - review & editing. **Wilfried Pacquentin**: Conceptualization, Supervision, Writing - review & editing. **Srikanth Narasimalu**: Conceptualization, Methodology, Supervision. **Hicham Maskrot**: Resources. **Fanny Balbaud-Celerier**: Conceptualization, Supervision, Writing - review & editing.

Bibliography

[1] J. Mou, X. Jia, P. Chen, L. Chen, Research on Operation Safety of Offshore Wind Farms, JMSE. 9 (2021) 881. https://doi.org/10.3390/jmse9080881.

[2] S. Musabikha, I.K. Utama, M. Mukhtasor, Corrosion in the Marine Renewable Energy: A Review, in: 2016.

[3] S.J. Price, R.B. Figueira, Corrosion Protection Systems and Fatigue Corrosion in Offshore Wind Structures: Current Status and Future Perspectives, Coatings. 7 (2017) 25. https://doi.org/10.3390/coatings7020025.

[4] R. Brijder, C.H.M. Hagen, A. Cortés, A. Irizar, U.C. Thibbotuwa, S. Helsen, S. Vásquez, A.P. Ompusunggu, Review of corrosion monitoring and prognostics in offshore wind turbine structures: Current status and feasible approaches, Frontiers in Energy Research. 10 (2022). https://www.frontiersin.org/articles/10.3389/fenrg.2022.991343 (accessed November 18, 2022).

[5] J. Bhandari, F. Khan, R. Abbassi, V. Garaniya, R. Ojeda, Modelling of pitting corrosion in marine and offshore steel structures – A technical review, Journal of Loss Prevention in the Process Industries. 37 (2015) 39–62. https://doi.org/10.1016/j.jlp.2015.06.008.

[6] P. Ernst, R.C. Newman, Pit growth studies in stainless steel foils. I. Introduction and pit growth kinetics, Corrosion Science. 44 (2002) 927–941. https://doi.org/10.1016/S0010-938X(01)00133-0.

[7] N.U. Obeyesekere, 9 - Pitting corrosion, in: A.M. El-Sherik (Ed.), Trends in Oil and Gas Corrosion Research and Technologies, Woodhead Publishing, Boston, 2017: pp. 215–248. https://doi.org/10.1016/B978-0-08-101105-8.00009-7.

[8] K. Eguchi, T.L. Burnett, D.L. Engelberg, X-Ray tomographic characterisation of pitting corrosion in lean duplex stainless steel, Corrosion Science. 165 (2020) 108406. https://doi.org/10.1016/j.corsci.2019.108406.
[9] J. Carroll, A. McDonald, D. McMillan, Failure rate, repair time and unscheduled O&M cost analysis of offshore wind turbines, Wind Energy. 19 (2016) 1107–1119. https://doi.org/10.1002/we.1887.
[10] P. Wen, Z. Cai, Z. Feng, G. Wang, Microstructure and mechanical properties of hot wire laser clad layers for repairing precipitation hardening martensitic stainless steel, Optics & Laser Technology. 75 (2015) 207–213. https://doi.org/10.1016/j.optlastec.2015.07.014.
[11] Standard ISO/ASTM 52900:2015. Additive Manufacturing – General Principles – Terminology, (2016).
[12] J.-H. Yu, Y.-S. Choi, D.-S. Shim, S.-H. Park, Repairing casting part using laser assisted additive metal-layer deposition and its mechanical properties, Optics & Laser Technology. 106 (2018) 87–93. https://doi.org/10.1016/j.optlastec.2018.04.007.
[13] W.J. Oh, Y. Son, S. Do Sik, Effect of in-situ heat treatments on deposition characteristics and mechanical properties for repairs using laser melting deposition, Journal of Manufacturing Processes. 58 (2020) 1019–1033. https://doi.org/10.1016/j.jmapro.2020.08.074.
[14] J.D. Hamilton, S. Sorondo, A. Greeley, X. Zhang, D. Cormier, B. Li, H. Qin, I.V. Rivero, Property-structure-process relationships in dissimilar material repair with directed energy deposition: Repairing gray cast iron using stainless steel 316L, Journal of Manufacturing Processes. 81 (2022) 27–34. https://doi.org/10.1016/j.jmapro.2022.06.015.
[15] A. Saboori, A. Aversa, G. Marchese, S. Biamino, M. Lombardi, P. Fino, Application of Directed Energy Deposition-Based Additive Manufacturing in Repair, Applied Sciences. 9 (2019) 3316. https://doi.org/10.3390/app9163316.
[16] X. Zhang, W. Li, X. Chen, W. Cui, F. Liou, Evaluation of component repair using direct metal deposition from scanned data, Int J Adv Manuf Technol. 95 (2018) 3335–3348. https://doi.org/10.1007/s00170-017-1455-y.
[17] X. Zhang, W. Cui, W. Li, F. Liou, A Hybrid Process Integrating Reverse Engineering, Pre-Repair Processing, Additive Manufacturing, and Material Testing for Component Remanufacturing, Materials. 12 (2019) 1961. https://doi.org/10.3390/ma12121961.
[18] Y. Li, Q. Han, I. Horváth, G. Zhang, Repairing surface defects of metal parts by groove machining and wire + arc based filling, Journal of Materials Processing Technology. 274 (2019) 116268. https://doi.org/10.1016/j.jmatprotec.2019.116268.
[19] W.J. Oh, W.J. Lee, M.S. Kim, J.B. Jeon, D.S. Shim, Repairing additive-manufactured 316L stainless steel using direct energy deposition, Optics & Laser Technology. 117 (2019) 6–17. https://doi.org/10.1016/j.optlastec.2019.04.012.
[20] J. Song, Q. Deng, C. Chen, D. Hu, Y. Li, Rebuilding of metal components with laser cladding forming, Applied Surface Science. 252 (2006) 7934–7940. https://doi.org/10.1016/j.apsusc.2005.10.025.
[21] B. Graf, A. Gumenyuk, M. Rethmeier, Laser Metal Deposition as Repair Technology for Stainless Steel and Titanium Alloys, Physics Procedia. 39 (2012) 376–381. https://doi.org/10.1016/j.phpro.2012.10.051.
[22] D. Liu, J. Lippold, J. Li, S. Rohklin, J. Vollbrecht, R. Grylls, Laser Engineered Net Shape (LENS) Technology for the Repair of Ni-Base Superalloy Turbine Components, Metallurgical and Materials Transactions A. 45 (2014). https://doi.org/10.1007/s11661-014-2397-8.
[23] H. Koehler, K. Partes, T. Seefeld, F. Vollertsen, Laser reconditioning of crankshafts: From lab to application, Physics Procedia. 5 (2010) 387–397. https://doi.org/10.1016/j.phpro.2010.08.160.
[24] J.M. Wilson, C. Piya, Y.C. Shin, F. Zhao, K. Ramani, Remanufacturing of turbine blades by laser direct deposition with its energy and environmental impact analysis, Journal of Cleaner Production. 80 (2014) 170–178. https://doi.org/10.1016/j.jclepro.2014.05.084.
[25] Q. Lai, R. Abrahams, W. Yan, C. Qiu, P. Mutton, A. Paradowska, M. Soodi, Investigation of a novel functionally graded material for the repair of premium hypereutectoid rails using laser cladding technology, Composites Part B: Engineering. 130 (2017) 174–191. https://doi.org/10.1016/j.compositesb.2017.07.089.

[26] K. Kanishka, B. Acherjee, A systematic review of additive manufacturing-based remanufacturing techniques for component repair and restoration, Journal of Manufacturing Processes. 89 (2023) 220–283. https://doi.org/10.1016/j.jmapro.2023.01.034.
[27] Standard Practice for Preparing, Cleaning, and Evaluating Corrosion Test Specimens, (n.d.). https://www.astm.org/g0001-03.html (accessed August 1, 2022).
[28] X. Zhang, W. Li, F. Liou, Damage detection and reconstruction algorithm in repairing compressor blade by direct metal deposition, Int J Adv Manuf Technol. 95 (2018) 2393–2404. https://doi.org/10.1007/s00170-017-1413-8.
[29] M. Hayajneh, M. Tahat, J. Bluhm, A Study of the Effects of Machining Parameters on the Surface Roughness in the End-Milling Process, in: 2007. https://www.semanticscholar.org/paper/A-Study-of-the-Effects-of-Machining-Parameters-on-Hayajneh-Tahat/5dd0c0273fe2c83c8052f8d6d3dc8583c3be23e7 (accessed January 4, 2023).
[30] M.H.M. Ghazali, A.Z.A. Mazlan, L.M. Wei, C.T. Tying, T.S. Sze, N.I.M. Jamil, Effect of Machining Parameters on the Surface Roughness for Different Type of Materials, IOP Conf. Ser.: Mater. Sci. Eng. 530 (2019) 012008. https://doi.org/10.1088/1757-899X/530/1/012008.
[31] Q. Zou, Robust and efficient tool path generation for poor-quality triangular mesh surface machining, Undefined. (2020). https://www.semanticscholar.org/reader/4aceab5265c3317363f35fb90e91d6fccd0b04f1 (accessed August 1, 2022).
[32] G. Urbikain, L.N.L. de Lacalle, Modelling of surface roughness in inclined milling operations with circle-segment end mills, Simulation Modelling Practice and Theory. 84 (2018) 161–176. https://doi.org/10.1016/j.simpat.2018.02.003.
[33] H. El Cheikh, B. Courant, S. Branchu, J.-Y. Hascoët, R. Guillén, Analysis and prediction of single laser tracks geometrical characteristics in coaxial laser cladding process, Optics and Lasers in Engineering. 50 (2012) 413–422. https://doi.org/10.1016/j.optlaseng.2011.10.014.
[34] D. Svetlizky, M. Das, B. Zheng, A.L. Vyatskikh, S. Bose, A. Bandyopadhyay, J.M. Schoenung, E.J. Lavernia, N. Eliaz, Directed energy deposition (DED) additive manufacturing: Physical characteristics, defects, challenges and applications, Materials Today. 49 (2021) 271–295. https://doi.org/10.1016/j.mattod.2021.03.020.
[35] T. Cailloux, W. Pacquentin, S. Narasimalu, F. Belnou, F. Schuster, H. Maskrot, C. Wang, K. Zhou, F. Balbaud-Celerier, Influence of trapezoidal groove geometry on the microstructure and mechanical properties of stainless steel 316L parts repaired by laser metal deposition, Materials Science and Engineering: A. (2022) 144218. https://doi.org/10.1016/j.msea.2022.144218.
[36] J. Hao, Q. Meng, C. Li, Z. Li, D. Wu, Effects of tilt angle between laser nozzle and substrate on bead morphology in multi-axis laser cladding, Journal of Manufacturing Processes. 43 (2019) 311–322. https://doi.org/10.1016/j.jmapro.2019.04.025.
[37] S. Bektas, Curvature of the Ellipsoid with Cartesian Coordinates, Landscape Architecture and Regional Planning. 2 (2017) 61. https://doi.org/10.11648/j.larp.20170202.13.
[38] ASTM, ASTM A276 - 10 Standard Specification for Stainless Steel Bars and Shapes, (2013). https://www.astm.org/DATABASE.CART/HISTORICAL/A276-10.htm (accessed March 30, 2021).
[39] H. Naesstroem, F. Brueckner, A.F.H. Kaplan, Blown powder directed energy deposition on various substrate conditions, Journal of Manufacturing Processes. 73 (2022) 660–667. https://doi.org/10.1016/j.jmapro.2021.11.048.
[40] ISO 25178-2:2012(en), Geometrical product specifications (GPS) — Surface texture: Areal — Part 2: Terms, definitions and surface texture parameters, (n.d.). https://www.iso.org/obp/ui/#iso:std:iso:25178:-2:ed-1:v1:en (accessed May 20, 2022).
[41] M.N. Ahsan, R. Bradley, A.J. Pinkerton, Microcomputed tomography analysis of intralayer porosity generation in laser direct metal deposition and its causes, Journal of Laser Applications. 23 (2011) 022009. https://doi.org/10.2351/1.3582311.
[42] L. Wang, P. Pratt, S.D. Felicelli, H. El Kadiri, J.T. Berry, P.T. Wang, M.F. Horstemeyer, Pore Formation in Laser-Assisted Powder Deposition Process, Journal of Manufacturing Science and Engineering. 131 (2009). https://doi.org/10.1115/1.3184087.

[43] B. Barkia, On the origin of the high tensile strength and ductility of additively manufactured 316L stainless steel: Multiscale investigation, Journal of Materials Science & Technology. 41 (2020) 209–218. https://doi.org/10.1016/j.jmst.2019.09.017.
[44] D. Kong, C. Dong, S. Wei, X. Ni, L. Zhang, R. Li, L. Wang, C. Man, X. Li, About metastable cellular structure in additively manufactured austenitic stainless steels, Additive Manufacturing. 38 (2021) 101804. https://doi.org/10.1016/j.addma.2020.101804.
[45] R.I. Revilla, M. Van Calster, M. Raes, G. Arroud, F. Andreatta, L. Pyl, P. Guillaume, I. De Graeve, Microstructure and corrosion behavior of 316L stainless steel prepared using different additive manufacturing methods: A comparative study bringing insights into the impact of microstructure on their passivity, Corrosion Science. 176 (2020) 108914. https://doi.org/10.1016/j.corsci.2020.108914.
[46] R.G. Thiessen, I.M. Richardson, A physically based model for microstructure development in a macroscopic heat-affected zone: Grain growth and recrystallization, Metall Mater Trans B. 37 (2006) 655–663. https://doi.org/10.1007/s11663-006-0050-7.
[47] Y. Balit, C. Guévenoux, A. Tanguy, M.V. Upadhyay, E. Charkaluk, A. Constantinescu, High resolution digital image correlation for microstructural strain analysis of a stainless steel repaired by Directed Energy Deposition, Materials Letters. 270 (2020) 127632. https://doi.org/10.1016/j.matlet.2020.127632.
[48] A.A. Voropaev, V.G. Protsenko, D.A. Anufriyev, M.V. Kuznetsov, A.A. Mukhin, M.N. Sviridenko, S.V. Kuryntsev, Influence of Laser Beam Wobbling Parameters on Microstructure and Properties of 316L Stainless Steel Multi Passed Repaired Parts, Materials. 15 (2022) 722. https://doi.org/10.3390/ma15030722.
[49] A.R. Kannan, S.M. Kumar, R. Pramod, N.S. Shanmugam, M. Vishnukumar, S. Naveenkumar, Microstructural characterization and mechanical integrity of stainless steel 316L clad layers deposited via wire arc additive manufacturing for nuclear applications, Materialwissenschaft Und Werkstofftechnik. 52 (2021) 617–623. https://doi.org/10.1002/mawe.202000242.
[50] Q. Auzoux, Fissuration en relaxation des aciers inoxydables austénitiques - Influence de l'écrouissage sur l'endommagement intergranulaire, phdthesis, École Nationale Supérieure des Mines de Paris, 2004. https://pastel.archives-ouvertes.fr/tel-00273520 (accessed October 28, 2021).
[51] S. Martínez, A. Lamikiz, E. Ukar, A. Calleja, J.A. Arrizubieta, L.N. Lopez de Lacalle, Analysis of the regimes in the scanner-based laser hardening process, Optics and Lasers in Engineering. 90 (2017) 72–80. https://doi.org/10.1016/j.optlaseng.2016.10.005.
[52] B. Zhou, P. Xu, W. Li, Y. Liang, Y. Liang, Microstructure and Anisotropy of the Mechanical Properties of 316L Stainless Steel Fabricated by Selective Laser Melting, Metals. 11 (2021) 775. https://doi.org/10.3390/met11050775.
[53] T.Y. Tsui, W.C. Oliver, G.M. Pharr, Influences of stress on the measurement of mechanical properties using nanoindentation: Part I. Experimental studies in an aluminum alloy, Journal of Materials Research. 11 (1996) 752–759. https://doi.org/10.1557/JMR.1996.0091.